TITLE

PDZD8 deficiency drives lipid accumulation in SNr and dopaminergic disinhibition

Running title

SNr lipid accumulation drives dopaminergic disinhibition

Authors

Tomoya Ozaki[1†], Yumi Morisugi[1†], Mei Kamino[1†], Hizuki Takahashi[1†], Honoka Maki[1], and Michiko Shirane[1]*

[1]Department of Molecular Biology, Graduate School of Pharmaceutical Sciences, Nagoya City University, Nagoya, Aichi, Japan

***Correspondence**

Michiko Shirane, shiram@phar.nagoya-cu.ac.jp

[†]These authors have contributed equally to this work and share first authorship

Keywords: Brain, Basal ganglia, Dopamine, SNr, Lipid, PDZD8, ADHD

ABSTRACT

The basal ganglia integrate cortical inputs to regulate motor, cognitive, and emotional behaviors through precisely balanced inhibitory and excitatory circuits. The substantia nigra pars reticulata (SNr) serves as a major output nucleus exerting tonic inhibition over thalamic and midbrain targets. However, how lipid metabolic disturbances affect SNr circuitry and dopaminergic regulation remains unclear. Here, we identify a crucial role for the lipid transport protein PDZD8 in maintaining basal ganglia circuit integrity. PDZD8 deficiency leads to marked lipid and lipofuscin accumulation selectively in the SNr, accompanied by enhanced striatal inhibitory inputs and reduced SNr projections to the ventromedial thalamus (VM) and midbrain dopaminergic nuclei (SNc, VTA). This circuit reorganization results in functional disinhibition and hyperactivation of dopaminergic neurons, producing maladaptive reinforcement of striatal inhibition. Our previous findings revealed that PDZD8$^{-/-}$ mice exhibit hyperactivity, reduced anxiety, and impaired fear memory, behavioral phenotypes reminiscent of attention-deficit/hyperactivity disorder (ADHD). These findings demonstrate that lipid accumulation in the SNr disrupts inhibitory output and dopaminergic regulation, forming a maladaptive basal ganglia–thalamocortical loop. Our study provides the first mechanistic link between lipid metabolic dysfunction, dopaminergic disinhibition, and ADHD-like behavioral phenotypes, highlighting PDZD8 as a key regulator of metabolic–circuit coupling in the basal ganglia.

INTRODUCTION

Basal ganglia and striatonigral pathway

The basal ganglia constitute a key component of the volitional motor system and contribute to essential aspects of cognition, sensorimotor integration, emotion, and learning. Dysfunction of basal ganglia circuits is implicated in a wide range of neurological and neuropsychiatric disorders(Park et al., 2020; Foster et al., 2021; McElvain et al., 2021). Current models describe three partially segregated channels of information flow through the basal ganglia—associative, limbic, and sensorimotor—which are further refined into multiple parallel subnetworks(Alexander et al., 1986; Grillner and Robertson, 2016). The cortico–basal ganglia–thalamic network (the basal ganglia–thalamocortical circuitry) represents one of the fundamental network motifs of the brain, consisting of precisely organized and reciprocally connected nodes(Foster et al., 2021; McElvain et al., 2021). Within this loop, the striatum, pallidum, and substantia nigra integrate widespread cortical inputs. The striatonigral (direct) pathway exhibits greater convergence than the striatopallidal (indirect) pathway, yet both ultimately converge onto the same output neurons within the substantia nigra pars reticulata (SNr), emphasizing the integrative nature of SNr-mediated control (Foster et al., 2021).

SNr as a major output nucleus of basal ganglia

SNr is the principal output nucleus of the basal ganglia, composed predominantly of inhibitory GABAergic neurons that project to specific thalamic nuclei and brainstem regions(Foster et al., 2021; McElvain et al., 2021; Falasconi et al., 2025). SNr neurons exhibit high tonic firing rates that maintain downstream targets under constant inhibition, whereas transient decreases in firing rate permit movement initiation via disinhibition. Recent studies have revealed that SNr neurons display multiphasic, bidirectional firing dynamics—both decreases and increases—allowing temporally precise modulation of downstream circuits during sequential motor acts(Falasconi et al., 2025). Notably, the caudal and lateral subregions of the SNr, which receive inputs from defined striatal territories, exhibit highly organized topographic projections(Lee et al., 2020; McElvain et al., 2021). These findings suggest that SNr subcircuits play specialized roles in coordinating movement and behavioral control.

SNr dysfunction and neuropsychiatric disorders

Attention-deficit/hyperactivity disorder (ADHD) is characterized by inattention, hyperactivity, and impulsivity, and is linked to altered dopaminergic and noradrenergic signaling(Biederman, 2005; Thapar and Cooper, 2016). Reduced cortical and subcortical gamma-amino butyric acid (GABA) levels have also been reported in ADHD. Among inhibitory neurons, parvalbumin-positive (PV^+) neurons play a key role in attentional

processes and motor control, and their dysfunction has been implicated in multiple psychiatric conditions, including schizophrenia, autism spectrum disorder, and ADHD(Lewis et al., 2005; Sohal et al., 2009). PV^+ neurons in the SNr provide critical feedforward inhibition and disinhibition within basal ganglia circuits. Recent work demonstrated that loss of histamine H_2 receptor (H_2R) expression in SNr PV^+ neurons leads to diminished neuronal activity and behavioral phenotypes resembling ADHD—hyperactivity, impulsivity, and inattention(Kim et al., 2016; Rizzi and Tan, 2019; An et al., 2025). Notably, this dysfunction in SNr PV^+ neurons, but not in medial prefrontal PV^+ neurons, was associated with elevated striatal dopamine levels, implicating the SNr as a key node in the dopaminergic dysregulation underlying ADHD(An et al., 2025).

Lipid metabolism and neuronal function

Lipid accumulation has long been associated with neurodegenerative conditions such as Alzheimer's disease (AD)(Dahm, 2006; Foley, 2010). The discovery of apolipoprotein E4 (ApoE4) as the strongest genetic risk factor for AD highlighted the importance of lipid metabolism in brain health(Lambert et al., 2013). Abnormal accumulation of cholesteryl esters (CEs)—neutral lipids involved in cholesterol transport—has been observed in brains of AD patients and AD model animals(van der Kant et al., 2019; Nugent et al., 2020; Blanchard et al., 2022; Litvinchuk et al., 2024). ApoE4-containing lipoproteins tend to aggregate within lysosomes, impairing degradation and promoting lipid peroxidation and inflammation. In neurons and glia carrying ApoE4, CEs accumulate in lysosomes and transform into lipofuscin, an autofluorescent granule composed of peroxidized lipids and damaged proteins that is highly resistant to degradation(Guo et al., 2025). Excessive lipofuscin accumulation leads to lysosomal stress and chronic neuroinflammation, processes increasingly recognized as drivers of neurodegeneration(Terman and Brunk, 2004; Gray and Woulfe, 2005; Moreno-Garcia et al., 2018).

PDZD8 and lipid homeostasis in the brain

We previously identified PDZD8 as a tethering protein at intracellular membrane contact sites (MCSs) between the endoplasmic reticulum (ER) and endosomes through proteomic analysis of the protrudin complex(Shirane and Nakayama, 2006; Shirane et al., 2020). PDZD8 belongs to the tubular lipid-binding (TULIP) superfamily and contains a synaptotagmin-like mitochondrial-lipid-binding (SMP) domain that mediates lipid transfer. We demonstrated that PDZD8 facilitates cholesterol transport(Shirane et al., 2020), and that PDZD8-deficient ($PDZD8^{-/-}$) mice exhibit brain-specific accumulation of CEs due to impaired lipophagy—a form of microautophagy in which lipid droplets directly fuse with lysosomes for degradation by lysosomal lipase(Morita et al., 2022). Behavioral battery analysis revealed that $PDZD8^{-/-}$ mice display pronounced

hyperactivity, reduced anxiety and fear, and deficits in fear-conditioned memory and working memory(Kurihara et al., 2023), collectively resembling ADHD-like phenotypes. Moreover, a PDZD8 mutation near the SMP domain has been linked to human intellectual disability, accompanied by regional brain hypertrophy and atrophy(Al-Amri et al., 2022).

Present study

Despite these findings, the specific brain regions and neural circuits affected by PDZD8 deficiency remained unclear. Here, we demonstrate that PDZD8$^{-/-}$ mice exhibit marked lipid accumulation in the SNr, a major output nucleus of the basal ganglia. This lipid deposition disrupts the striato–nigro–thalamo–cortical circuitry, leading to disinhibition of dopaminergic neurons and maladaptive reinforcement of striatal inhibitory feedback. These results provide the first evidence that abnormal lipid metabolism in the SNr can remodel basal ganglia circuits, offering new insights into the mechanistic links between lipid dysregulation, dopaminergic imbalance, and ADHD-like behavioral phenotypes.

RESULTS

PDZD8 expression in midbrain neurons and astrocytes

To determine the cellular distribution of PDZD8, we examined its expression in the midbrain of wild-type mice. PDZD8 was abundantly expressed in SNc, VTA, and SNr, regions defined by dopamine transporter (DAT) expression (Figure 1A). In the SNc and VTA, PDZD8 was localized in DAT- and tyrosine hydroxylase (TH)-positive dopaminergic neurons, respectively (Figure 1B, C). In contrast, PDZD8 was expressed in PV-positive GABAergic neurons and glial fibrillary acidic protein (GFAP)-positive astrocytes within the SNr (Figure 1D, E). These findings indicate that PDZD8 is highly distributed across neuronal and glial populations around the substantia nigra in midbrain, suggesting its potential role in modulating dopaminergic circuitry.

Marked lipid accumulation in SNr in PDZD8$^{-/-}$ mice

Given that PDZD8$^{-/-}$ mice exhibit abnormal CE accumulation in the brain, we next identified the affected brain regions. LipiDye II staining revealed significant lipid accumulation in several areas, including SNr, dorsal raphe (DR), basolateral amygdala (BLA), and central amygdala (CeA), with the SNr showing the most prominent signal (Figure 2A). These results were confirmed by LipiDye II and LipidTOX staining (Figure 2B, C). High-resolution Z-stack imaging demonstrated dense intracellular lipid droplets, likely representing lipofuscin, within SNr cells (Figure 2D). Thus, the SNr represents the principal site of lipid deposition in PDZD8$^{-/-}$ mice.

Lipofuscin deposits are enriched in SNr in PDZD8$^{-/-}$ mice

To characterize the lipid deposits in greater detail, serial midbrain sections were stained

with LipiDye II and anti-DAT. Large lipid deposits were concentrated in the caudal SNr, while smaller aggregates appeared rostrally (Figure 3A). Ectopic anti-DAT signals were detected in PDZD8$^{-/-}$ SNr, especially in caudal regions, likely overlapping with LipiDye II fluorescence (Figure 3B). Then triple labeling with LipiDye II, DAT, and GFAP confirmed complete overlap of these signals, consistent with autofluorescent lipofuscin (Figure 3C). These results demonstrate that most large lipid deposits in the caudal SNr of PDZD8$^{-/-}$ brain are lipofuscin.

Extracellular and intracellular lipid deposits in SNr in PDZD8$^{-/-}$ mice

Z-stack 3D imaging combined with GFAP staining revealed two types of lipid deposits in the SNr of PDZD8-/- mice: small extracellular deposits, likely lipoproteins, and large intracellular deposits, likely lipofuscin (Figure 4A–C). Extracellular deposits were more abundant medially, while intracellular deposits predominated laterally. 3D reconstructions further distinguished intra- versus extracellular localization (Supplementary movies A, B). Notably, intracellular lipofuscin overlapped with GFAP signals, suggesting autofluorescent properties of astrocytic lipofuscin.

Enhanced striatal projection to SNr in PDZD8$^{-/-}$ mice

To test whether lipid accumulation alters SNr connectivity, we performed retrograde neural tracing by injecting Alexa-CTb into the SNr of PDZD8$^{+/+}$ and PDZD8$^{-/-}$ mice (Figure 5A, B). In both genotypes, injection sites were equivalent. However, corpus striatal (CP) neurons, including pallidum (GP) neurons, projecting to SNr were markedly increased and spatially expanded in PDZD8$^{-/-}$ mice (Figure 5C, D). These changes indicate enhanced striatal inputs to the SNr (Figure 5E). PDZD8 expression was also detected in dopamine- and cAMP-regulated phosphoprotein (DARPP-32)-positive medium spiny neurons (MSNs) in the striatum (Figure 5F), and DARPP-32 immunoreactivity was significantly elevated in the SNr of PDZD8$^{-/-}$ mice (Figure 5G). Together, these findings suggest strengthened GABAergic striatal inputs to SNr in PDZD8 deficiency.

Abnormal dopaminergic circuits in PDZD8$^{-/-}$ mice

Given that SNr serves as a major output nucleus of the basal ganglia that regulates both thalamic and midbrain dopaminergic neurons, we examined downstream projections using palmitoylated GFP (palGFP) injections into the SNr of PDZD8$^{+/+}$ and PDZD8$^{-/-}$ mice (Figure 6A, B). Injection sites were comparable between groups. In PDZD8$^{-/-}$ mice, projections from the SNr to the VM and nst (Figure 6C), as well as to the VTA and SNc (Figure 6D), were markedly reduced compared to controls, indicating disrupted SNr output (Figure 6E).

Based on these observations, we propose that lipid accumulation in the SNr induces

functional disinhibition within the basal ganglia–thalamocortical circuitry (Figure 6F). Specifically, lipid deposition in SNr neurons leads to reduced inhibitory output from the SNr to both VM and the nst, as well as to the VTA and SNc. The consequent disinhibition of thalamic and dopaminergic targets results in hyperactivation of dopaminergic neurons, which in turn enhances inhibitory feedback from striatal GABAergic neurons to SNr, thereby reinforcing the suppression of SNr output. This establishes a maladaptive feedback loop—reduced SNr–thalamic output, dopaminergic disinhibition, and strengthened striatal inhibition—that possibly destabilizes the functional balance of the basal ganglia–thalamocortical circuitry. Such large-scale circuit dysregulation likely underlies the abnormal behavioral phenotypes observed in PDZD8$^{-/-}$ mice, including hyperactivity, reduced anxiety and fear, and impaired fear-memory regulation.

DISCUSSION

Summary of the findings

In this study, we identified a crucial role of the lipid transport protein PDZD8 in maintaining basal ganglia circuit homeostasis. PDZD8 deficiency led to prominent lipid accumulation in the SNr, accompanied by structural and functional remodeling of basal ganglia output pathways. Neuronal tracing analyses revealed reduced SNr projections to both thalamic (VM, nst) and midbrain dopaminergic targets (VTA, SNc), together with enhanced inhibitory input from striatal GABAergic neurons. These anatomical changes were consistent with functional disinhibition of dopaminergic circuits, resulting in hyperactivation of dopaminergic neurons and maladaptive reinforcement of striatal inhibition. Given that PDZD8$^{-/-}$ mice exhibit hyperactivity and reduced anxiety and fear at the behavioral level—features reminiscent of ADHD-like phenotypes—these findings establish a direct mechanistic link between lipid metabolic disruption in the SNr, basal ganglia circuit disinhibition, and behavioral dysregulation.

SNr lipid accumulation and circuit disinhibition

The SNr serves as a tonic inhibitory gate in the cortico–basal ganglia–thalamo–cortical loop (basal ganglia–thalamocortical circuit), controlling both motor and cognitive outputs. Our data suggest that lipid accumulation within SNr neurons compromises this inhibitory control, likely by affecting cellular excitability and synaptic output. Lipofuscin-like deposits, enriched in cholesteryl esters and peroxidized lipids, are known to induce lysosomal stress, oxidative imbalance, and altered membrane conductance. These effects may collectively reduce the firing capacity or GABA release efficacy of SNr neurons, thereby reducing inhibitory output to their downstream targets. The observed reduction of SNr projections to VM and nst implies a loss of inhibitory tone at the thalamic level,

which would increase cortical excitability and contribute to hyperactivity. Similarly, decreased inhibition of VTA and SNc dopaminergic neurons produces dopaminergic disinhibition, leading to excessive dopamine release in the striatum. The resulting dopaminergic hyperactivation enhances corticostriatal drive, which strengthens striatal GABAergic feedback to the SNr. This closed-loop maladaptive feedback—SNr hypoactivity, dopaminergic hyperactivation, and enhanced striatal inhibition—creates a self-reinforcing circuit instability. Such loop-level dysregulation likely underlies the behavioral abnormalities observed in PDZD8$^{-/-}$ mice.

Disinhibition-driven distortion of RPE signaling in the VTA–BLA circuit

Beyond basal ganglia output pathways, the disinhibition of dopaminergic neurons observed in PDZD8$^{-/-}$ mice likely extends its impact to broader reward-related networks, particularly the VTA–BLA circuit, which encodes reward prediction error (RPE) signals during associative learning. The VTA conveys phasic dopamine release to the BLA during both appetitive and aversive conditioning, where dopaminergic modulation shapes the associative strength between conditioned and unconditioned stimuli. Disruption of inhibitory control from the SNr to midbrain dopaminergic neurons may bias RPE computation—amplifying positive prediction signals while diminishing aversive or omission-related responses. Such imbalance could account for the hyperactivity and impaired fear memory observed in PDZD8$^{-/-}$ mice, reflecting aberrant valuation of outcomes and a failure to encode negative prediction errors. In this framework, lipid accumulation–induced disinhibition of the SNr may distort dopaminergic gain control within the VTA–BLA network, leading to maladaptive reinforcement learning and emotional dysregulation. This suggests that PDZD8-dependent lipid homeostasis in the SNr is essential for maintaining the dynamic balance between positive and negative RPE signaling across cortico–amygdalo–dopaminergic loops.

Comparison with prior studies on basal ganglia and ADHD

Our findings extend previous evidence implicating SNr dysfunction in the pathophysiology of ADHD. Earlier studies demonstrated that H_2R deficiency in PV$^+$ neurons of the SNr reduces inhibitory output and induces hyperactivity and impulsivity. Similarly, reduced GABAergic tone and enhanced dopaminergic transmission have been reported in ADHD patients and model animals. The present work suggests that lipid metabolic stress may represent a previously unrecognized upstream mechanism producing a similar disinhibitory outcome. PDZD8 is an ER–endosome tethering protein required for lipid transport and membrane contact site integrity. Loss of PDZD8 impairs lipophagy, leading to intracellular lipid droplet accumulation and lipofuscin formation. These pathological deposits are not inert: they alter calcium handling, disrupt

mitochondrial dynamics, and perturb synaptic vesicle turnover. The convergence of metabolic and electrophysiological dysfunction in SNr neurons likely explains the observed circuit-level changes. Therefore, disinhibition of SNr neurons emerges as a new paradigm linking lipid homeostasis to dopaminergic regulation and behavioral control.

Regulation of inhibitory circuits by lipid metabolism

Lipid homeostasis is increasingly recognized as a determinant of neuronal function. Our findings highlight that inhibitory GABAergic circuits are particularly sensitive to metabolic stress. The SNr, characterized by high tonic firing rates, may be especially vulnerable to disruptions in lipid trafficking and degradation. Accumulation of peroxidized lipids and lipofuscin can impair GABA release machinery and ion channel stability, thereby compromising tonic inhibition. Astrocytic PDZD8 expression observed in our study suggests that glia–neuron lipid coupling may be essential for maintaining SNr function. Disruption of such glial lipid buffering could amplify local oxidative stress and propagate dysfunction across the basal ganglia network.

Implications for neuropsychiatric and neurodegenerative disorders

The link between lipid accumulation and circuit disinhibition identified here may have broader implications beyond ADHD. Lipofuscin accumulation and lysosomal dysfunction are hallmarks of Alzheimer's disease and aging-related cognitive decline. The present findings suggest that even in the absence of overt neurodegeneration, lipid metabolic perturbations can remodel inhibitory circuits and alter behavioral state. Given the prominent dopaminergic involvement, PDZD8 dysfunction may represent a shared vulnerability factor bridging metabolic stress, dopamine dysregulation, and cognitive-behavioral disorders.

Limitation of the study

Although PDZD8 is broadly expressed across multiple brain regions, prominent lipid accumulation occurred selectively in the SNr of PDZD8$^{-/-}$ mice. The regional vulnerability underlying this selectivity remains unresolved and warrants further investigation, including the potential involvement of PDZD8-interacting complex components. Future studies combining in vivo imaging of dopamine dynamics, electrophysiological recordings of SNr neurons, and cell-type–specific PDZD8 rescue in neuronal versus glial populations will be essential to delineate the relative contributions of each cell type. Moreover, pharmacological or genetic interventions aimed at restoring lipid homeostasis may help determine whether normalization of lipid metabolism can rescue basal ganglia circuit stability and behavioral deficits.

Conclusion

Together, our findings reveal that PDZD8-dependent lipid metabolism is indispensable

294 for preserving inhibitory control within the basal ganglia and ensuring accurate
295 dopaminergic prediction error signaling, providing a unifying mechanistic framework
296 linking metabolic stress, circuit disinhibition, and behavioral dysregulation.
297
298 **METHODS**
299 **Animals**
300 Mice were housed under 12-h light/dark cycle with food and water ad libitum. All
301 mouse experiments were approved by the animal ethics committee of Nagoya City
302 University.
303 **Mutant mice**
304 Generation of PDZD8-KO mice was described previously(Morita et al., 2022). In brief,
305 Cas9 nickase mRNA, Generic tracrRNA, and target-specific crRNA were mixed and
306 injected into C57BL/6J mouse zygotes. The resultant mutant mice were backcrossed
307 with C57BL/6J mice before experiments. Animals were genotyped by PCR analysis.
308 **Antibodies and reagents**
309 Rabbit polyclonal antibodies to PDZD8 were from Sigma-Aldrich; mouse monoclonal
310 antibodies to TH were from Sigma-Aldrich; mouse monoclonal antibodies to GFAP
311 were from Proteintech; guinea pig polyclonal antibodies to DAT, PV, and DARPP were
312 from Frontier institute; Alexa Fluor 488 goat anti-rabbit IgG, Alexa Fluor 555 goat anti-
313 mouse IgG, Alexa Fluor 555 goat anti-guinea pig IgG, LipidTox, and Alexa Fluor 594
314 cholera toxin B were from Thermo Fisher Scientific; LipiDye II was from Funakoshi.
315 **Immunohistofluorescence analysis**
316 Mouse brain was fixed with 2% paraformaldehyde in phosphate-buffered saline (PBS,
317 Wako), exposed consecutively to 15% and 30% sucrose in PBS for 2 days, and
318 embedded in tissue-Tek OCT compound (SAKURA). Thin sections were prepared with
319 a cryostat microtome (CM1850 UV, Leica) and stained consecutively with primary
320 antibodies and Alexa Fluor–labeled secondary antibodies in PBS containing 0.5% Triton
321 X-100, or stained with LipiDye II or LipidTox in PBS. The sections were observed with
322 an LSM800 confocal microscope (Zeiss), and the images were processed for calculation
323 of fluorescence intensity with ZEN imaging software (Zeiss). Brain regions were
324 referenced from Allen Brain Atlas (http://atlas.brain-map.org).
325 **Stereotaxic injection**
326 Mice were anesthetized intraperitoneally with a mixture of midazolam (4 mg kg^{-1},
327 SANDOZ, Tokyo, Japan), medetomidine (0.75 mg kg^{-1}, Kyoritsu Seiyaku, Tokyo,
328 Japan) and butorphanol (5 mg kg^{-1}, Meiji Seika Pharma, Tokyo, Japan) and placed in a
329 stereotaxic frame (NARISHIGE, Tokyo, Japan). Body temperature was maintained at

37 °C. The scalp was sterilized and incised, and a small craniotomy was made above the target. Alexa Fluor 594–conjugated cholera toxin subunit B (Thermo Fisher Scientific, MA, USA) was prepared at 2 μg μL^{-1} in sterile PBS. AAV2-CMV-palGFP virus particles were from Dr. Nakamura(Yahiro et al., 2023). Tracer (200 nL per site) was delivered using a Hamilton microsyringe (1701RN Neuros Syringe, 33G; Hamilton Company, NV, USA) connected to a motorized stereotaxic microinjector (NARISHIGE, Tokyo, Japan ; 100 nL min^{-1}). After infusion, the needle was left in place for 10–15 min to minimize reflux before being withdrawn slowly. For each mouse, injections were made at the following stereotaxic coordinates relative to bregma: [AP -3.2], [ML ±1.4], [DV -4.4] (mm). The scalp was closed with sutures, and mice were monitored until full recovery. After surgery, mice received postoperative care including an intraperitoneal injection of antibiotic (amoxicillin, Kyoritsu Seiyaku, Tokyo, Japan; 50 mg kg^{-1}, i.p.).

Statistical analysis

Statistical analysis was performed with the use of BellCurve for Excel software (Social Survey Research Information, Tokyo, Japan). Normality of data was assessed with the Shapiro-Wilk test. If the normality was not met, the Mann-Whitney U test was applied (Fig. A, SNr; DR; BLA). If data were normally distributed and variance was homogeneous between genotypes, comparisons were performed with Student's *t* test. If homogeneity of variance was not assumed, Welch's *t* test was applied instead of Student's *t* test (Fig. A, CeA). Quantitative data are presented as mean ± SE. Statistical significance of a *P* value is indicated as $p < 0.001$ (***). Sample size (n) are in the figure legends.

Acknowledgements

We thank K. Nakamura for AAV2-CMV-palGFP virus particles, I. Yamahata for Immunohistofluorescence analysis, and the Research Equipment Sharing Center at Nagoya City University for assistance.

Author contributions statement

M.S. conceptualized and supervised the study, acquired funding, designed experiments, and wrote the manuscript; T.O., Y.M., M.K., and H.T. performed experiments; H.M. prepared resources.

Funding information

This work was supported in part by KAKENHI grants from Japan Society for the

Promotion of Science (JSPS) to M.S. (24K02122).

Ethics

The animal study was approved by Nagoya City University, Animal Research Committee. The study was conducted in accordance with the local legislation and institutional requirements.

Data availability and sources

The original contributions presented in the study are included in the article/ supplementary material, further inquiries can be directed to the corresponding author.

REFERENCES

Al-Amri, A.H., Armstrong, P., Amici, M., Ligneul, C., Rouse, J., El-Asrag, M.E., et al. (2022). PDZD8 Disruption Causes Cognitive Impairment in Humans, Mice, and Fruit Flies. *Biol Psychiatry* 92(4)**,** 323-334. doi: 10.1016/j.biopsych.2021.12.017.

Alexander, G.E., DeLong, M.R., and Strick, P.L. (1986). Parallel organization of functionally segregated circuits linking basal ganglia and cortex. *Annu Rev Neurosci* 9**,** 357-381. doi: 10.1146/annurev.ne.09.030186.002041.

An, D., You, Y., Ma, Q., Xu, Z., Liu, Z., Liao, R., et al. (2025). Deficiency of histamine H(2) receptors in parvalbumin-positive neurons leads to hyperactivity, impulsivity, and impaired attention. *Neuron* 113(4)**,** 572-589 e576. doi: 10.1016/j.neuron.2024.12.002.

Biederman, J. (2005). Attention-deficit/hyperactivity disorder: a selective overview. *Biol Psychiatry* 57(11)**,** 1215-1220. doi: 10.1016/j.biopsych.2004.10.020.

Blanchard, J.W., Akay, L.A., Davila-Velderrain, J., von Maydell, D., Mathys, H., Davidson, S.M., et al. (2022). APOE4 impairs myelination via cholesterol dysregulation in oligodendrocytes. *Nature* 611(7937)**,** 769-779. doi: 10.1038/s41586-022-05439-w.

Dahm, R. (2006). Alzheimer's discovery. *Curr Biol* 16(21)**,** R906-910. doi: 10.1016/j.cub.2006.09.056.

Falasconi, A., Kanodia, H., and Arber, S. (2025). Dynamic basal ganglia output signals license and suppress forelimb movements. *Nature* 644(8077)**,** 749-758. doi: 10.1038/s41586-025-09066-z.

Foley, P. (2010). Lipids in Alzheimer's disease: A century-old story. *Biochim Biophys Acta* 1801(8)**,** 750-753. doi: 10.1016/j.bbalip.2010.05.004.

Foster, N.N., Barry, J., Korobkova, L., Garcia, L., Gao, L., Becerra, M., et al. (2021). The

402 mouse cortico-basal ganglia-thalamic network. *Nature* 598(7879), 188-194. doi:
403 10.1038/s41586-021-03993-3.
404 Gray, D.A., and Woulfe, J. (2005). Lipofuscin and aging: a matter of toxic waste. *Sci*
405 *Aging Knowledge Environ* 2005(5), re1. doi: 10.1126/sageke.2005.5.re1.
406 Grillner, S., and Robertson, B. (2016). The Basal Ganglia Over 500 Million Years. *Curr*
407 *Biol* 26(20), R1088-R1100. doi: 10.1016/j.cub.2016.06.041.
408 Guo, J.L., Braun, D., Fitzgerald, G.A., Hsieh, Y.T., Rouge, L., Litvinchuk, A., et al. (2025).
409 Decreased lipidated ApoE-receptor interactions confer protection against
410 pathogenicity of ApoE and its lipid cargoes in lysosomes. *Cell* 188(1), 187-206
411 e126. doi: 10.1016/j.cell.2024.10.027.
412 Kim, H., Ahrlund-Richter, S., Wang, X., Deisseroth, K., and Carlen, M. (2016). Prefrontal
413 Parvalbumin Neurons in Control of Attention. *Cell* 164(1-2), 208-218. doi:
414 10.1016/j.cell.2015.11.038.
415 Kurihara, Y., Mitsunari, K., Mukae, N., Shoji, H., Miyakawa, T., and Shirane, M. (2023).
416 PDZD8-deficient mice manifest behavioral abnormalities related to emotion,
417 cognition, and adaptation due to dyslipidemia in the brain. *Mol Brain* 16(1), 11.
418 doi: 10.1186/s13041-023-01002-4.
419 Lambert, J.C., Ibrahim-Verbaas, C.A., Harold, D., Naj, A.C., Sims, R., Bellenguez, C., et
420 al. (2013). Meta-analysis of 74,046 individuals identifies 11 new susceptibility
421 loci for Alzheimer's disease. *Nat Genet* 45(12), 1452-1458. doi: 10.1038/ng.2802.
422 Lee, J., Wang, W., and Sabatini, B.L. (2020). Anatomically segregated basal ganglia
423 pathways allow parallel behavioral modulation. *Nat Neurosci* 23(11), 1388-1398.
424 doi: 10.1038/s41593-020-00712-5.
425 Lewis, D.A., Hashimoto, T., and Volk, D.W. (2005). Cortical inhibitory neurons and
426 schizophrenia. *Nat Rev Neurosci* 6(4), 312-324. doi: 10.1038/nrn1648.
427 Litvinchuk, A., Suh, J.H., Guo, J.L., Lin, K., Davis, S.S., Bien-Ly, N., et al. (2024).
428 Amelioration of Tau and ApoE4-linked glial lipid accumulation and
429 neurodegeneration with an LXR agonist. *Neuron* 112(3), 384-403 e388. doi:
430 10.1016/j.neuron.2023.10.023.
431 McElvain, L.E., Chen, Y., Moore, J.D., Brigidi, G.S., Bloodgood, B.L., Lim, B.K., et al.
432 (2021). Specific populations of basal ganglia output neurons target distinct brain
433 stem areas while collateralizing throughout the diencephalon. *Neuron* 109(10),
434 1721-1738 e1724. doi: 10.1016/j.neuron.2021.03.017.
435 Moreno-Garcia, A., Kun, A., Calero, O., Medina, M., and Calero, M. (2018). An
436 Overview of the Role of Lipofuscin in Age-Related Neurodegeneration. *Front*
437 *Neurosci* 12, 464. doi: 10.3389/fnins.2018.00464.

Morita, K., Wada, M., Nakatani, K., Matsumoto, Y., Hayashi, N., Yamahata, I., et al. (2022). PDZD8-deficient mice accumulate cholesteryl esters in the brain as a result of impaired lipophagy. *iScience* 25(12), 105612. doi: 10.1016/j.isci.2022.105612.

Nugent, A.A., Lin, K., van Lengerich, B., Lianoglou, S., Przybyla, L., Davis, S.S., et al. (2020). TREM2 Regulates Microglial Cholesterol Metabolism upon Chronic Phagocytic Challenge. *Neuron* 105(5), 837-854 e839. doi: 10.1016/j.neuron.2019.12.007.

Park, J., Coddington, L.T., and Dudman, J.T. (2020). Basal Ganglia Circuits for Action Specification. *Annu Rev Neurosci* 43, 485-507. doi: 10.1146/annurev-neuro-070918-050452.

Rizzi, G., and Tan, K.R. (2019). Synergistic Nigral Output Pathways Shape Movement. *Cell Rep* 27(7), 2184-2198 e2184. doi: 10.1016/j.celrep.2019.04.068.

Shirane, M., and Nakayama, K.I. (2006). Protrudin induces neurite formation by directional membrane trafficking. *Science* 314(5800), 818-821. doi: 10.1126/science.1134027.

Shirane, M., Wada, M., Morita, K., Hayashi, N., Kunimatsu, R., Matsumoto, Y., et al. (2020). Protrudin and PDZD8 contribute to neuronal integrity by promoting lipid extraction required for endosome maturation. *Nat Commun* 11(1), 4576. doi: 10.1038/s41467-020-18413-9.

Sohal, V.S., Zhang, F., Yizhar, O., and Deisseroth, K. (2009). Parvalbumin neurons and gamma rhythms enhance cortical circuit performance. *Nature* 459(7247), 698-702. doi: 10.1038/nature07991.

Terman, A., and Brunk, U.T. (2004). Lipofuscin. *Int J Biochem Cell Biol* 36(8), 1400-1404. doi: 10.1016/j.biocel.2003.08.009.

Thapar, A., and Cooper, M. (2016). Attention deficit hyperactivity disorder. *Lancet* 387(10024), 1240-1250. doi: 10.1016/S0140-6736(15)00238-X.

van der Kant, R., Langness, V.F., Herrera, C.M., Williams, D.A., Fong, L.K., Leestemaker, Y., et al. (2019). Cholesterol Metabolism Is a Druggable Axis that Independently Regulates Tau and Amyloid-beta in iPSC-Derived Alzheimer's Disease Neurons. *Cell Stem Cell* 24(3), 363-375 e369. doi: 10.1016/j.stem.2018.12.013.

Yahiro, T., Kataoka, N., and Nakamura, K. (2023). Two Ascending Thermosensory Pathways from the Lateral Parabrachial Nucleus That Mediate Behavioral and Autonomous Thermoregulation. *J Neurosci* 43(28), 5221-5240. doi: 10.1523/JNEUROSCI.0643-23.2023.

475 **FIGURE LEGENDS**

476 **Figure 1. PDZD8 is highly expressed in neurons and astrocytes in the midbrain.**
477 Immunofluorescence analysis of wild-type mouse brain.
478 (A) Dopamine transporter (DAT, magenta) and PDZD8 (green) in the midbrain. Regions
479 corresponding to substantia nigra pars compacta (SNc), ventral tegmental area (VTA),
480 and substantia nigra pars reticulata (SNr) are indicated in the DAT image. The merged
481 image is also shown. Scale bars, 200 μm.
482 (B) PDZD8 (green) and DAT (magenta) in SNc.
483 (C) PDZD8 (green) and tyrosine hydroxylase (TH, magenta) in VTA.
484 (D) PDZD8 (green) and parvalbumin (PV, magenta) in SNr.
485 (E) PDZD8 (green) and GFAP (magenta) in SNr. Scale bars, 20 μm (B–E).
486

487 **Figure 2. Lipofuscin deposits are markedly increased in SNr in PDZD8$^{-/-}$ mice.**
488 Lipid aggregate analysis of PDZD8$^{+/+}$ and PDZD8$^{-/-}$ mouse brains.
489 (A) Dot plots showing mean fluorescence intensity of LipiDye II in SNr, dorsal raphe
490 (DR), basolateral amygdala (BLA), and central amygdala (CeA). Schematic brain
491 sections indicate the regions analyzed. Red lines in sagittal sections (upper) indicate the
492 positions of coronal sections (lower), and red boxes mark the analyzed regions.
493 (B, C) Confocal images of LipiDye II (B) and LipidTox (C) in SNr. Boxed regions (left)
494 are shown at higher magnification (right). Scale bars, 50 μm (left) and 20 μm (right).
495 (D) High-resolution images of LipiDye II in SNr of PDZD8$^{-/-}$ mice. Boxed regions (left)
496 are shown enlarged (right). A differential interference contrast (DIC) image is also
497 shown. The dotted line outlines a cell periphery densely packed with lipofuscin (right).
498 Scale bars, 5 μm.
499

500 **Figure 3. Lipofuscin deposits are enriched in SNr in PDZD8$^{-/-}$ mice.**
501 Lipid aggregate analysis of SNr in PDZD8$^{+/+}$ and PDZD8$^{-/-}$ mouse brains.
502 (A) Confocal images of DAT (magenta) and LipiDye II (green) in serial sections of SNr
503 from rostral (left) to caudal (right) regions at 240 μm intervals. Scale bars, 100 μm. For
504 PDZD8-/-, enlarged images of LipiDye II are also shown. Scale bars, 20 μm.
505 (B) The merged images of DAT and DIC for the images outlined in (A) in PDZD8$^{+/+}$
506 and PDZD8$^{-/-}$. The merged images of LipiDye II and DIC in PDZD8$^{-/-}$ are also shown.
507 Scale bars, 100 μm.
508 (C) Confocal images of LipiDye II (green), DAT (blue), and GFAP (magenta) in SNr in
509 PDZD8$^{-/-}$. The merged image is also shown. Scale bars, 20 μm.
510

511 **Figure 4. Extracellular and intracellular lipid deposits in SNr in PDZD8-/- mice.**
512 (A) Scheme of coronal section containing SNr from mouse brain atlas (left), in which
513 SNr is shown enlarged (right) with the medial (M) and lateral (L) regions indicated.
514 (B, C) 3D images of LipiDye II (green) and GFAP (magenta) in medial (B) and lateral
515 (C) regions of SNr in PDZD8$^{-/-}$ mice, which are reconstructed from z-stack confocal
516 images using Imaris software. Scale bars, 10 μm.
517
518 **Figure 5. Abnormal striatal projection to SNr in PDZD8$^{-/-}$ mice.**
519 (A, B) Confocal images of Alexa-conjugated cholera toxin subunit B (Alexa-CTb)
520 injected to SNr merged with DIC images. Tiling image of cerebral hemisphere (A) and
521 serial sections from rostral (left) to caudal (right) regions at 50 μm intervals focusing on
522 SNr (B). Scale bars, 500 μm (A) and 200 μm (B).
523 (C, D) Confocal images of Alexa-CTb merged with DIC images of brain region
524 containing striatum, indicating projection sources. Tiling image of cerebral hemisphere
525 (C) and serial sections from rostral (left) to caudal (right) regions at 50 μm intervals
526 focusing on striatum (D). Scale bars, 500 μm (A) and 200 μm (B).
527 (E) Schematic representation of striatal projections to SNr, with showing increase in
528 PDZD8$^{-/-}$ mice compared to PDZD8$^{+/+}$ mice. Injection sites of CTb to SNr are also
529 indicated.
530 (F) Immunofluorescence images of PDZD8 (green) and dopamine- and cAMP-regulated
531 phosphoprotein (DARPP-32, magenta) in striatum of wild-type mice, with merged
532 image. Scale bars, 20 μm.
533 (G) Immunofluorescence images of DARPP and merged with DIC in SNr of PDZD8$^{+/+}$
534 and PDZD8$^{-/-}$. Scale bars, 100 μm.
535
536 **Figure 6. Abnormal dopaminergic circuits in PDZD8$^{-/-}$ mice.**
537 (A, B) Confocal images showing palmitoylated GFP (palGFP) injection sites in SNr
538 merged with DIC images. Tiling image of cerebral hemisphere (A) and serial sections
539 from rostral (left) to caudal (right) regions at 100 μm intervals focusing on SNr (B).
540 Scale bars, 500 μm (A); 200 μm (B).
541 (C) Confocal and merged DIC images of thalamic regions showing SNr projection
542 targets. PalGFP signals indicate projections to the ventromedial thalamus (VM) and the
543 nigrostriatal tract (nst). Scale bars, 200 μm.
544 (D) Confocal and merged DIC images of midbrain regions showing SNr projections to
545 the ventral tegmental area (VTA) and substantia nigra pars compacta (SNc). Scale bars,
546 200 μm.

(E) Schematic illustration summarizing the anterograde tracing results. Projections from the SNr to both VM/nst and VTA/SNc are markedly reduced in PDZD8$^{-/-}$ mice compared with PDZD8$^{+/+}$ mice. Injection sites of palGFP in the SNr are indicated.
(F) Proposed circuit model depicting the consequences of lipid accumulation in the SNr of PDZD8$^{-/-}$ mice. In PDZD8$^{+/+}$ mice (left), striatal GABAergic inputs transiently inhibit SNr neurons, which tonically suppress activity in thalamic (VM/nst) and midbrain dopaminergic (VTA/SNc) targets, maintaining balanced inhibitory control within the basal ganglia–thalamocortical circuit. In PDZD8$^{-/-}$ mice (right), lipid accumulation in SNr neurons reduces their inhibitory output to VM/nst and VTA/SNc, resulting in functional disinhibition of thalamic and dopaminergic pathways. The consequent hyperactivation of dopaminergic neurons increases dopamine release in the striatum, thereby enhancing inhibitory feedback from striatal neurons to the SNr. This establishes a maladaptive feedback loop—reduced SNr–thalamic output, dopaminergic hyperactivation, and strengthened striatal inhibition—that destabilizes the functional balance of the basal ganglia–thalamocortical circuit and underlies the ADHD-like behavioral abnormalities observed in PDZD8$^{-/-}$ mice.

SUPPLEMENTARY FIGURE LEGENDS

Supplementary movie. 3D movies of lipid deposits in SNr in PDZD8$^{-/-}$ mice.
(A, B) 3D movies of LipiDye II (green) and GFAP (magenta) in medial (A) and lateral (B) regions of SNr in PDZD8$^{-/-}$ mice, which are corresponding to Figure 4B and C, respectively. Scale bars, 10 μm.

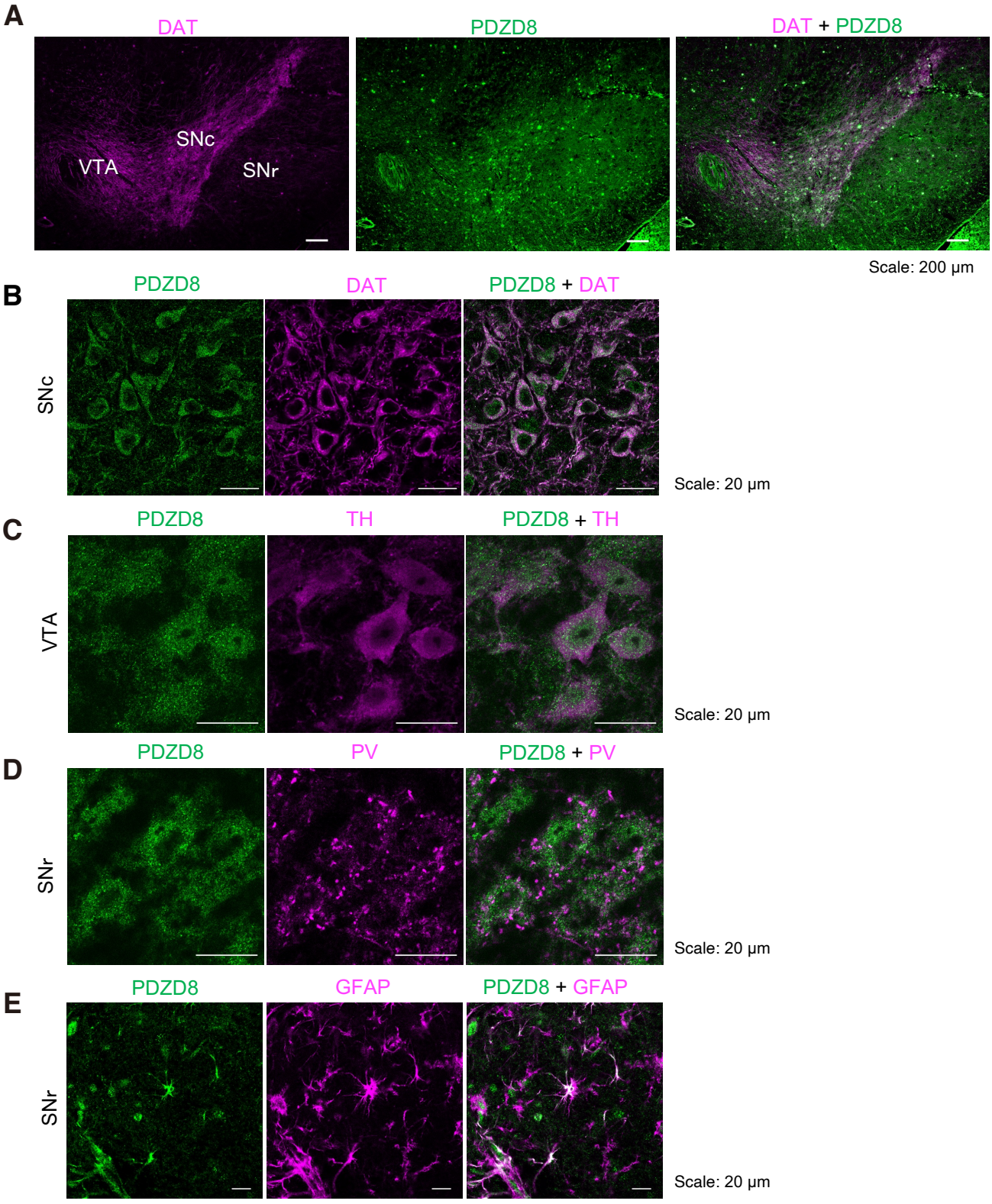
A
DAT
PDZD8
DAT + PDZD8
SNc
VTA
SNr
Scale: 200 μm
B
PDZD8
DAT
PDZD8 + DAT
SNc
Scale: 20 μm
C
PDZD8
TH
PDZD8 + TH
VTA
Scale: 20 μm
D
PDZD8
PV
PDZD8 + PV
SNr
Scale: 20 μm
E
PDZD8
GFAP
PDZD8 + GFAP
SNr
Scale: 20 μm

Figure 1

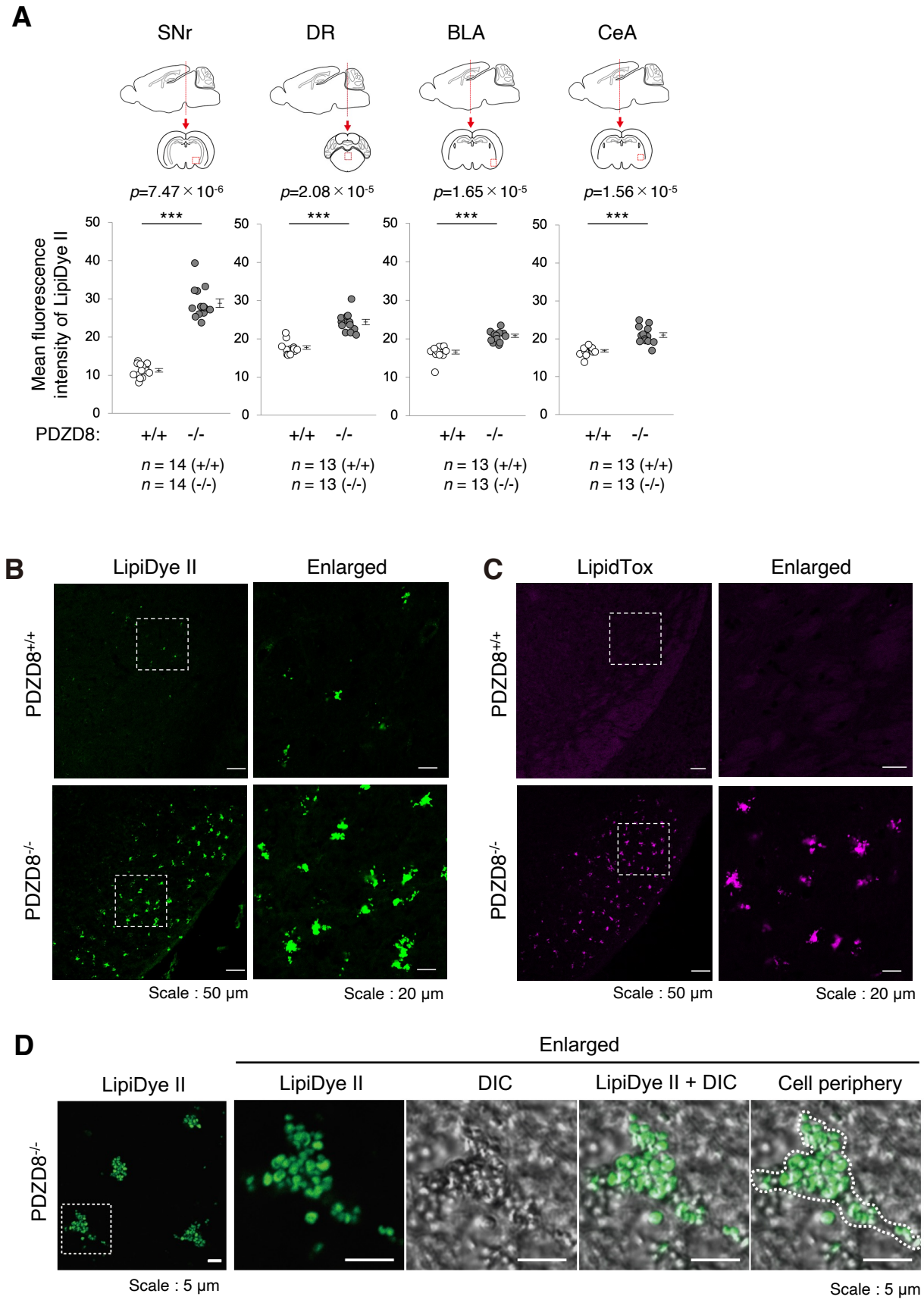
A
SNr
DR
BLA
CeA
p=7.47 × 10-6
p=2.08 × 10-5
p=1.65 × 10-5
p=1.56 × 10-5
***
Mean fluorescence intensity of LipiDye II
PDZD8:
+/+
-/-
n = 14 (+/+)
n = 14 (-/-)
n = 13 (+/+)
n = 13 (-/-)
B
LipiDye II
Enlarged
PDZD8+/+
PDZD8-/-
Scale : 50 μm
Scale : 20 μm
C
LipidTox
Enlarged
PDZD8+/+
PDZD8-/-
Scale : 50 μm
Scale : 20 μm
D
Enlarged
LipiDye II
LipiDye II
DIC
LipiDye II + DIC
Cell periphery
PDZD8-/-
Scale : 5 μm
Scale : 5 μm

Figure 2

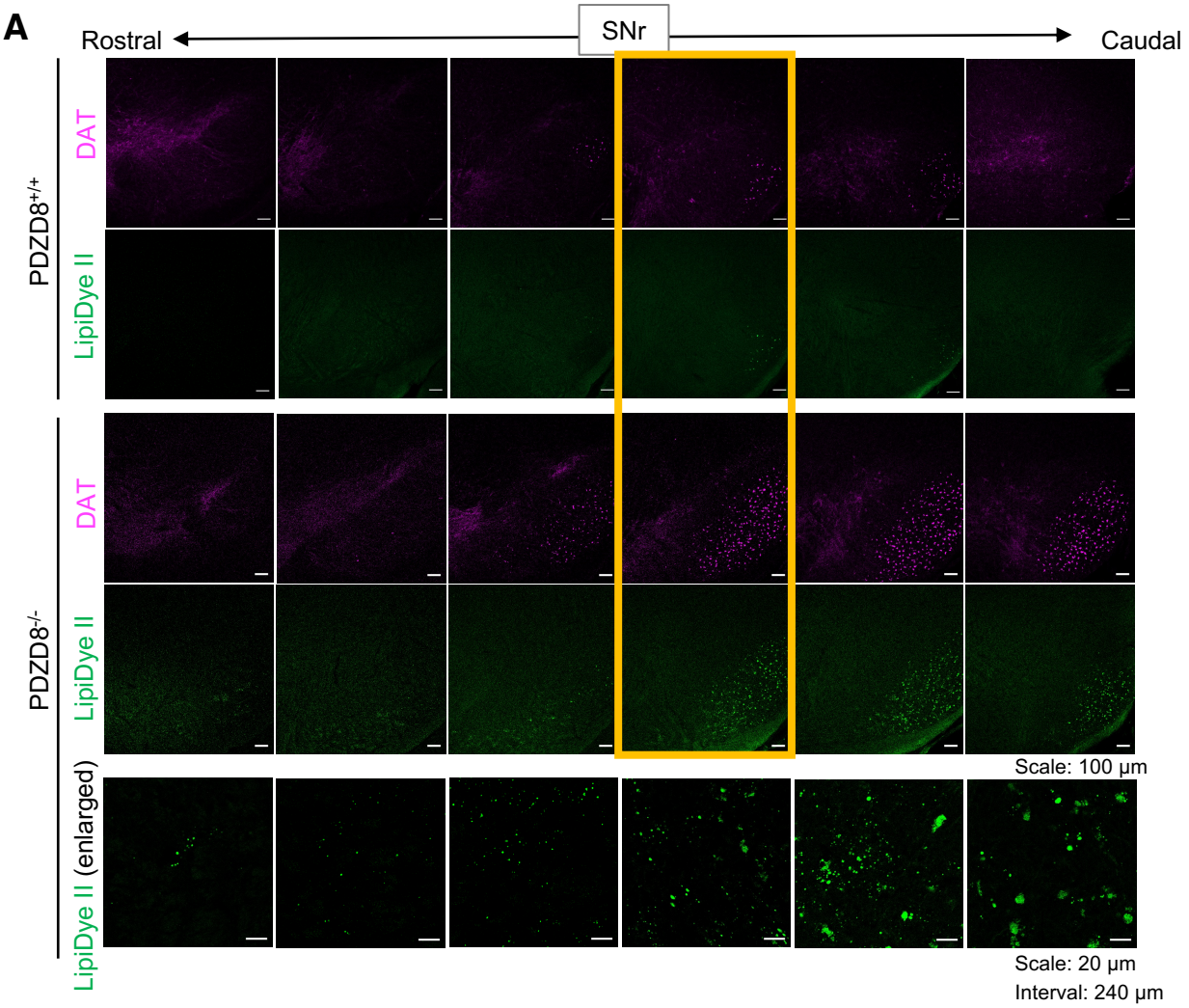
A
Rostral
SNr
Caudal
PDZD8+/+
DAT
LipiDye II
PDZD8-/-
DAT
LipiDye II
LipiDye II (enlarged)
Scale: 100 μm
Scale: 20 μm
Interval: 240 μm

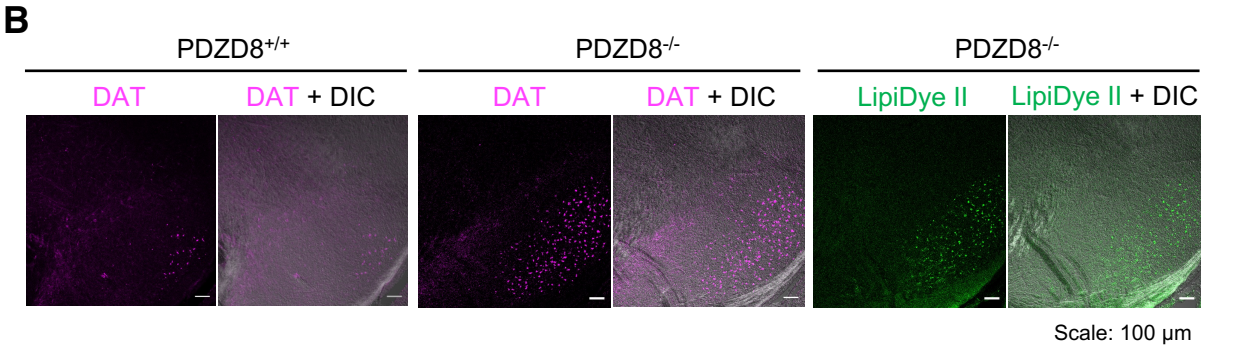
B
PDZD8+/+
PDZD8-/-
PDZD8-/-
DAT
DAT + DIC
DAT
DAT + DIC
LipiDye II
LipiDye II + DIC
Scale: 100 μm

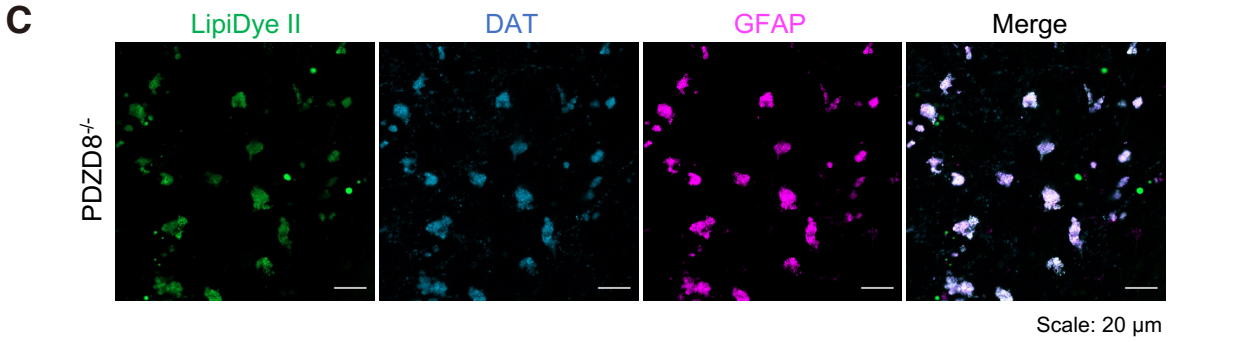
C
LipiDye II
DAT
GFAP
Merge
PDZD8-/-
Scale: 20 μm

Figure 3

A

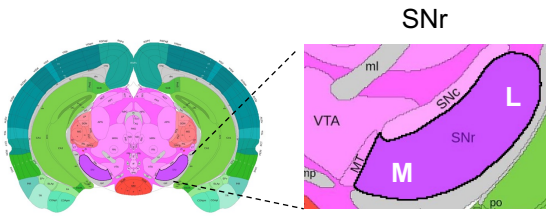

B

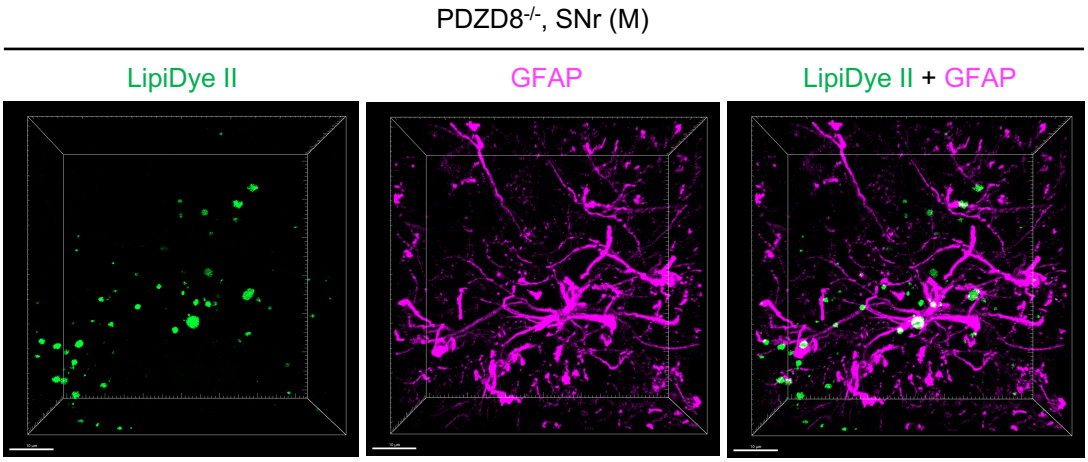

Scale: 10 μm

C

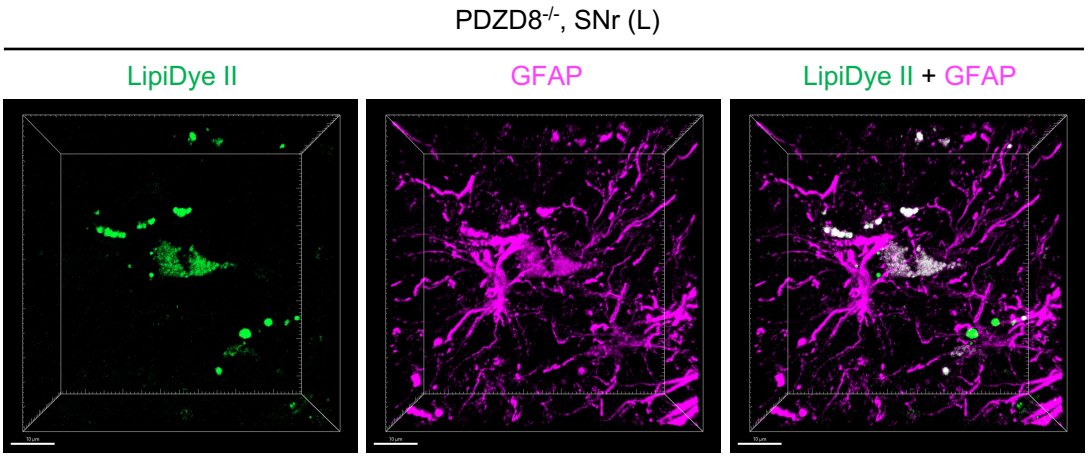

Scale: 10 μm

Figure 4

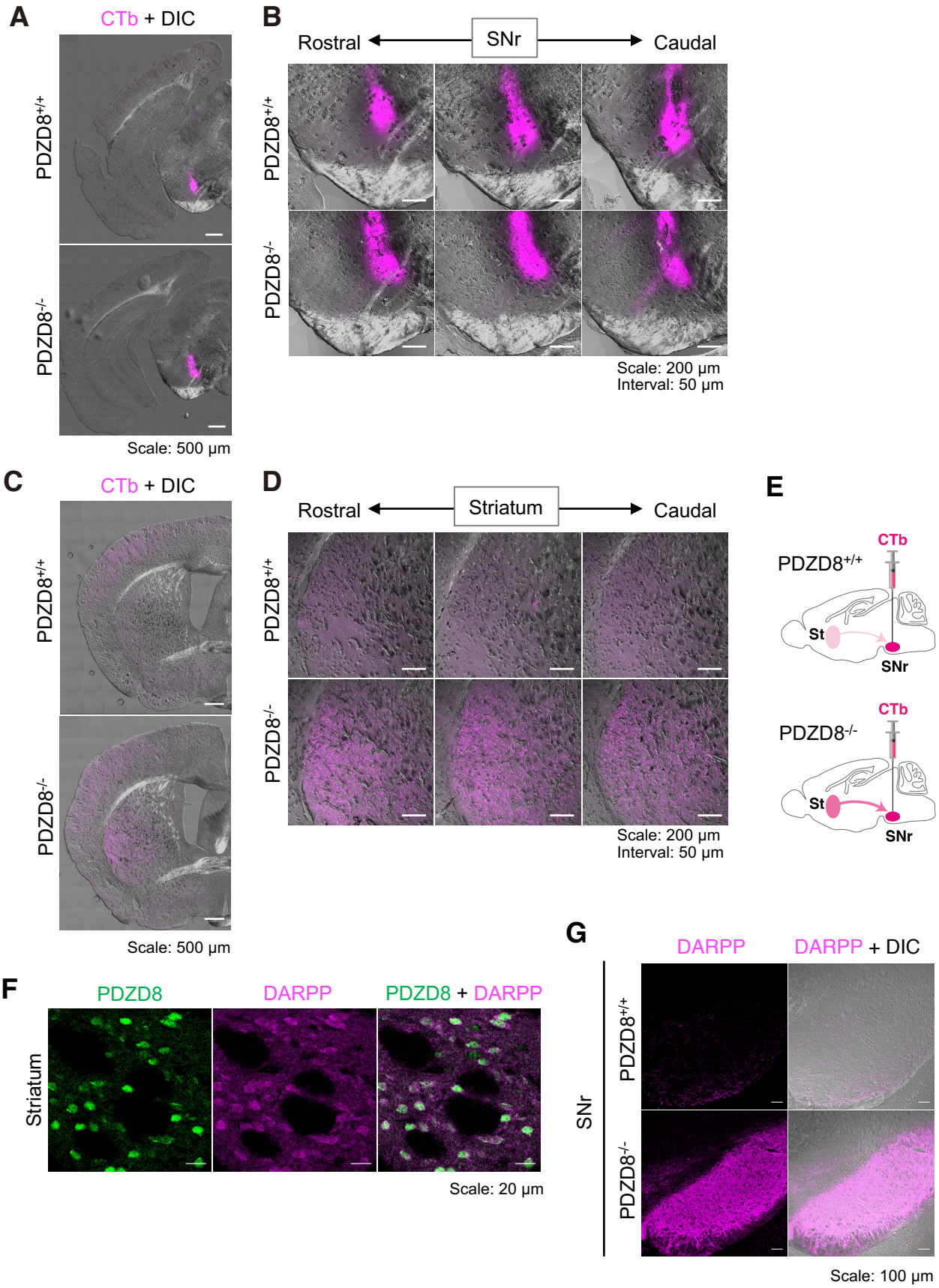
A
CTb + DIC
PDZD8+/+
PDZD8-/-
Scale: 500 µm
B
Rostral
SNr
Caudal
PDZD8+/+
PDZD8-/-
Scale: 200 µm
Interval: 50 µm
C
CTb + DIC
PDZD8+/+
PDZD8-/-
Scale: 500 µm
D
Rostral
Striatum
Caudal
PDZD8+/+
PDZD8-/-
Scale: 200 µm
Interval: 50 µm
E
CTb
PDZD8+/+
St
SNr
CTb
PDZD8-/-
St
SNr
F
PDZD8
DARPP
PDZD8 + DARPP
Striatum
Scale: 20 µm
G
DARPP
DARPP + DIC
SNr
PDZD8+/+
PDZD8-/-
Scale: 100 µm

Figure 5

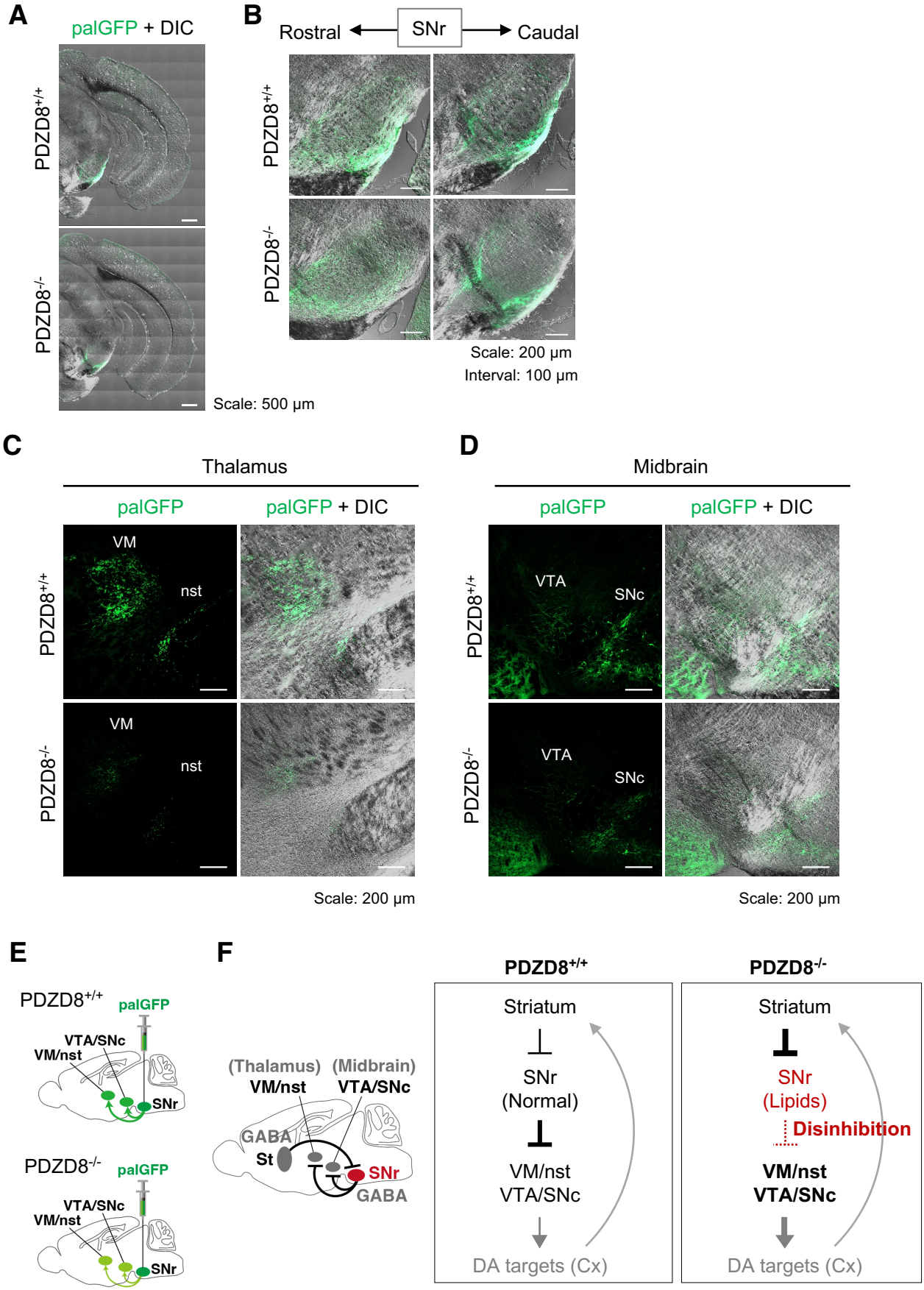
A
palGFP + DIC
PDZD8+/+
PDZD8-/-
Scale: 500 μm
B
Rostral
SNr
Caudal
PDZD8+/+
PDZD8-/-
Scale: 200 μm
Interval: 100 μm
C
Thalamus
palGFP
palGFP + DIC
VM
nst
PDZD8+/+
PDZD8-/-
Scale: 200 μm
D
Midbrain
palGFP
palGFP + DIC
VTA
SNc
PDZD8+/+
PDZD8-/-
Scale: 200 μm
E
PDZD8+/+
palGFP
VTA/SNc
VM/nst
SNr
PDZD8-/-
palGFP
VTA/SNc
VM/nst
SNr
F
(Thalamus)
(Midbrain)
VM/nst
VTA/SNc
GABA
St
SNr
GABA
PDZD8+/+
Striatum
SNr
(Normal)
VM/nst
VTA/SNc
DA targets (Cx)
PDZD8-/-
Striatum
SNr
(Lipids)
Disinhibition
VM/nst
VTA/SNc
DA targets (Cx)

Figure 6